

# Nanoporous Copper Ribbons Prepared by Chemical Dealloying of a Melt-Spun ZnCu Alloy

Sawsan Ibrahim, Alexandra Dworzak, Daniel Crespo, Frank Uwe Renner, Carsten Dosche, and Mehtap Oezaslan\*



Cite This: *J. Phys. Chem. C* 2022, 126, 212–226



Read Online

ACCESS |



Metrics & More

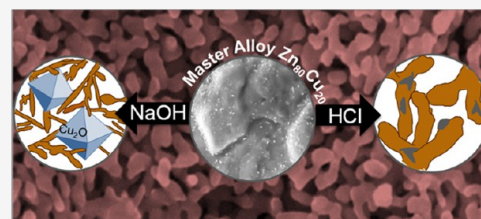


Article Recommendations



Supporting Information

**ABSTRACT:** Dealloying is a powerful and versatile method to fabricate three-dimensional nanoporous (np) materials with high surface area. In this work, we investigated the dealloying processes of Zn<sub>80</sub>Cu<sub>20</sub> alloy ribbons in acidic and alkaline environments. Our results show that the nanostructure can be controlled by varying the nature of electrolyte solution, pH value, dealloying time, and temperature. In acidic media, the presence of chloride ions enhances the Cu surface mobility, leading to a faster coarsening and growth of ligaments during the dealloying process over time. In contrast, the surface diffusivity of Cu atoms in alkaline media is three orders lower than that in acid and results in a remarkably smaller ligament size due to the formation of Cu (hydr)oxide surface species. Cross-section analysis indicates that the dealloying process is largely controlled by interfacial processes. Interestingly, local Zn-rich regions were found near the surface in np-Cu ribbons dealloyed in 0.1 M HCl. This comprehensive study shows the influence of dealloying conditions on the morphology and residual Zn content of np-Cu ribbons as a model system for fabricating bicontinuous ligament-pore network materials with tailored structural and chemical properties for applications in electrochemical synthesis, sensors, and catalysis.



## 1. INTRODUCTION

Nanoporous (np) materials present a three-dimensional and self-assembled network of solid ligaments and pores with scale length ranging from a few nanometers to tens of micrometers.<sup>1</sup> They have particular properties, such as high surface area, large number of low-coordinated surface atoms, and enhanced mass transport properties.<sup>1–3</sup> Therefore, they show promising applications in several areas including catalysis,<sup>2,4</sup> energy storage,<sup>5,6</sup> surface-enhanced Raman scattering (SERS),<sup>7,8</sup> and electrochemical sensors.<sup>9</sup> Np-materials can be fabricated by templating or dealloying methods. The first involves the use of porous sacrificial molds or templates, on which metals can be deposited. Either inorganic (hard templating) or polymeric (soft templating) templates are used. The templates are then removed to form a metal replica of the template structure.<sup>10</sup> Although this method provides a precise control of porosity, it can be highly time-consuming and experimentally very complex based on numerous steps.

On the other hand, dealloying is considered as a powerful and versatile synthetic route to fabricate np-materials, which has extensively been applied in the last two decades.<sup>11–13</sup> The dealloying process includes a selective dissolution of less noble metal from an alloy, either chemically or electrochemically.<sup>14</sup> The evolution of bicontinuous ligament-pore structure is based on the critical interplay between the dissolution rate of less noble metal and the surface diffusion rate of remaining noble metal at the alloy–electrolyte interface.<sup>12,13</sup> The different microstructure evolution characteristics of obtained np-materi-

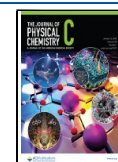
al during dealloying process can be controlled by varying the electrolyte and dealloying time.<sup>15,16</sup> The tunable content of less noble metal in np-materials prepared by dealloying adds the advantage of changing the electronic and geometric properties of the noble metal-rich materials.<sup>17</sup> For example, it has been reported that residual Ag content strongly influences the SERS effects of np-Au prepared from dealloying of Ag–Au master alloys.<sup>18</sup>

The evolution of np-Au from Ag–Au alloy has been investigated in numerous studies.<sup>19–21</sup> Pt-based np materials have also been the focus of many studies as promising catalysts for fuel cell applications, such as np-Pt and np-Au–Cu–Pt films.<sup>22,23</sup> Np-Cu has attracted attention as a cheaper material. It has many interesting applications in the field of catalysis,<sup>17</sup> sensors,<sup>24</sup> and batteries.<sup>25</sup> For instance, Cu-based catalysts are used in fuel and chemical production processes such as production of methanol and water-gas shift reaction.<sup>16,26</sup> The first application of a dealloying process to fabricate np-Cu was Raney's copper, a widely used catalyst in water-gas shift reaction, that was prepared by dealloying of Al–Cu alloy.<sup>16</sup> Later, various binary alloys have been used to form np-Cu via

**Received:** September 19, 2021

**Revised:** December 14, 2021

**Published:** December 29, 2021



dealloying process including Al–Cu,<sup>27</sup> Ti–Cu,<sup>28</sup> Mn–Cu,<sup>29</sup> Mg–Cu,<sup>30</sup> and Zn–Cu.<sup>31,32</sup>

Generally, the master alloy has a great impact on the properties of dealloyed np structures. Alloys can be manufactured using different techniques including melt spinning,<sup>29</sup> quenching of molten metals,<sup>33</sup> and electrodeposition of less noble metals followed by thermal annealing.<sup>17</sup> This might form different crystal phase structures, homogeneities, and thicknesses of master alloys, and hence influences the resulting dealloyed structure. Mn<sub>70</sub>Cu<sub>30</sub> alloys prepared by two different processes, arc and quench melting, have shown different oxide inclusions and second phases, which contribute to different homogeneity of the np structure.<sup>33</sup> The morphology of np-Cu could also be affected by different annealing temperatures used to form Zn–Cu alloy films after electrodeposition of Zn layer on a Cu substrate.<sup>31</sup> Not only the alloy formation method, but also the elemental ratio of initial alloy influences the kinetics of the dealloying process as well as the morphology of the resulting np-Cu.<sup>16,34</sup> As another interesting example, partial dealloying of Au<sub>40</sub>Cu<sub>28</sub>Ag<sub>7</sub>Pd<sub>5</sub>Si<sub>20</sub> ribbons (25 μm thick) in 1 M HNO<sub>3</sub> has shown an inhomogeneous structure between the surface and cross-section of the ribbons.<sup>35</sup> This observation might be attributed to the dealloying front propagation process and its fundamental mechanism for these alloy ribbons. Two different mechanisms during dealloying are discussed in the literature, the interfacial mechanism and the long-range mass transport mechanism. The interfacial mechanism is based on the different kinetics of surface diffusion of the remaining noble metal atoms and selective dissolution of the less noble metal atoms at the alloy–electrolyte interface, while the long-range transport mechanism is controlled by diffusion of aggressive electrolyte solution and corrosion product in and out of the porous metal layer. Thus, the evolution of a three-dimensional porous structure from melt-spun Cu alloy ribbons is not well explored in the literature.

In addition to the master alloy, the nature of electrolyte plays a critical role in the dealloying process. It might be associated with the different dealloying rates and surface mobilities of Cu atoms depending on the environment.<sup>17,33</sup> Different np-Cu morphologies and dealloying mechanisms have been reported in alkaline and acidic media.<sup>17,27,36</sup> For instance, the nature of anions has also shown a significant influence on the ligament size. Chloride ions are able to enhance Cu surface diffusivity, leading to increase of ligament size, whereas the presence of phosphate ions shows an inhibition effect and thus much smaller ligament size.<sup>16,37</sup> All in all, there are many experimental factors to control and modify the structural and chemical properties of the resulting np-materials via dealloying.

This study aims to look deeper into the development of ligament-pore network on the surface and cross-section of np-Cu ribbons, formed by chemical dealloying of melt-spun Zn<sub>80</sub>Cu<sub>20</sub> ribbons in 0.1 M HCl and 1.3 M NaOH solutions. Here, the effects of the dealloying conditions on the structure and residual Zn content of np-Cu ribbons have intensively been investigated by varying the nature of electrolyte, dealloying time, temperature, de-aeration, and agitation of the electrolyte solution. This allows us to gain better understanding of the dealloying process for fabricating np-Cu ribbons with tailored structural and chemical properties for applications in electrochemical synthesis, sensors and catalysis.

## 2. EXPERIMENTAL METHODS

**2.1. Fabrication of Zn<sub>80</sub>Cu<sub>20</sub> Alloy Ribbons.** Ribbons were prepared via melt spinning process (Edmund Buehler, melt spinner SC, Germany). The chamber was evacuated to 10<sup>−3</sup> mbar and then filled with Ar (99.995%, Nippon Gases) to a pressure of 0.4 bar. Pure copper (99.99%, Alfa Aesar) and zinc (99.9%, Alfa Aesar) as foils were melted at ~850 K for 1 min, avoiding any Zn evaporation. A mass of 5–10 g per run was ejected onto a cold rotating copper disk operated at a cooling rate of 10<sup>5</sup> to 10<sup>6</sup> K s<sup>−1</sup>. The geometric dimensions of as-prepared Zn<sub>80</sub>Cu<sub>20</sub> ribbons were 4–10 cm long, 2–3 mm wide, and 35 ± 3 μm thick, respectively.

**2.2. Chemical Dealloying of Zn<sub>80</sub>Cu<sub>20</sub> Alloy Ribbons.** Before the dealloying process, the pristine ribbons were cleaned with highly purified water (18 MΩ cm at room temperature, Elga PureLab Classic) and propan-2-ol (99.5%, Fisher Scientific) using an ultrasonication bath. 0.1 M hydrochloric acid (HCl) and 1.3 M sodium hydroxide (NaOH) were used as electrolyte solutions prepared by diluting 37% HCl (VWR Chemicals) or by dissolving the respective amount of NaOH pellets (99.99%, Alfa Aesar) in highly purified water, respectively. Both solutions were saturated with Ar (99.999%, Air Liquide) for at least 30 min. Ribbons were chemically dealloyed in 25 mL vials at several temperatures under an Ar atmosphere using a bath thermostat (Lauda, ECO RE620). Only in 1.3 M NaOH, the ribbons were attached to a Cu foil (0.1 mm thick, 99.999%, Alfa Aesar) to accelerate the Zn dissolution. Treated samples were taken out from the solution after different dealloying times (3.5, 8, 24, 48, 72, 92, 168, and 312 h). They were washed with highly purified water, dried in an Ar atmosphere and immediately used for further investigations or stored in vacuum to avoid air oxidation. All experiments were repeated at least 3 times.

**2.3. Scanning Electron Microscopy Equipped with Energy-Dispersive X-ray Spectroscopy.** The structure, morphology, and chemical composition of pristine and dealloyed ribbons were investigated using a Helios NanoLab 600i scanning electron microscopy (SEM) (operated at an accelerating voltage of 5 kV and a current of 0.17 nA) equipped with an Apollo 10 energy-dispersive X-ray spectroscopy (EDX) detector (EDAX AMETEK) and the Everhart–Thornley secondary electron detector. For top-view SEM images, aluminum flat FIB pin mounts (12.7 mm diameter) were used to mount the samples. The cross-section acquisitions were carried out by putting the samples vertically on a 90° FIB pin mount so that the cross-section of the samples were in the optical zone of the beam. Micrographs were acquired at a working distance of 4.0 mm and a dwell time of 30 μs. Sample areas were imaged in a magnification range from 1500× to 200,000×. ImageJ 1.46r software was then used to establish the ligament sizes of np-material samples from numerous SEM micrographs by analyzing more than 200 arbitrary ligaments. For the elemental quantification, the characteristic intensities of the K line for O, Cu, and Zn at 0.525, 6.924, and 8.630 keV were evaluated, respectively. Each measurement was repeated at least three times for each sample.

**2.4. High Resolution (Scanning) Transmission Electron Microscopy.** A JEOL JEM2100F microscope operating at accelerating voltage of 200 kV and equipped with an Oxford INCA Energy TEM 250 EDX system with a silicon drift detector was employed to investigate the morphology and chemical composition of np-Cu ribbons at higher magnifica-

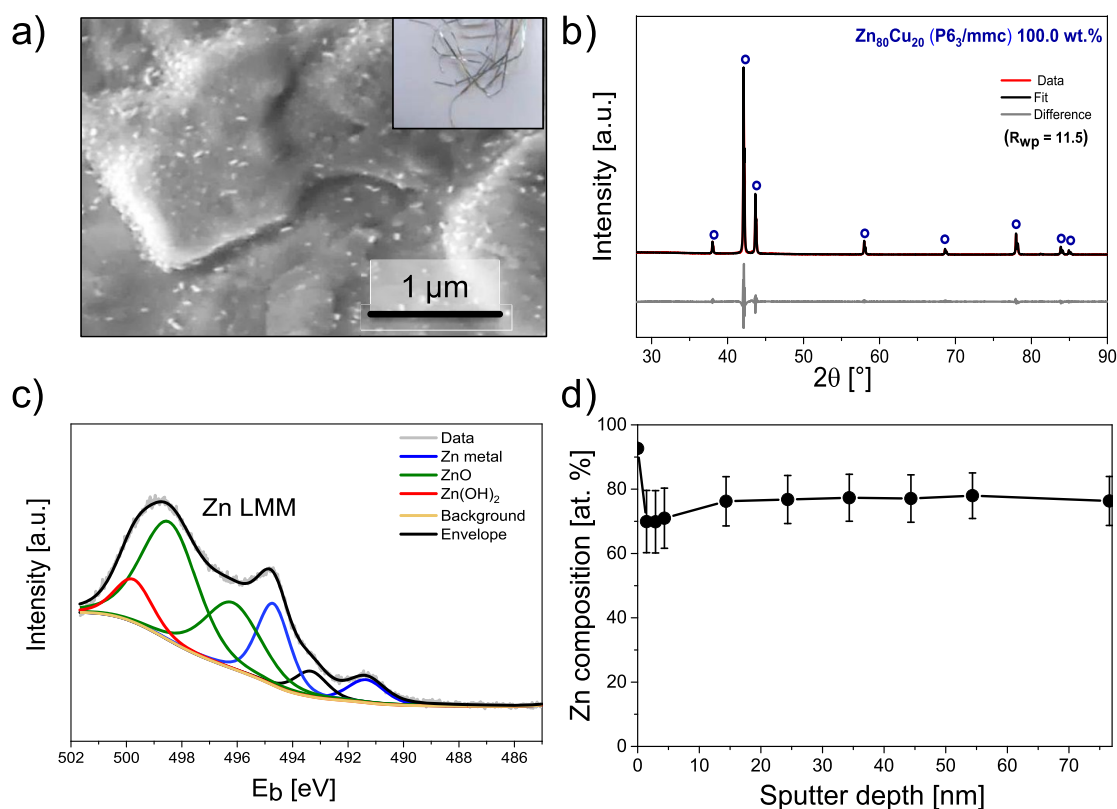


**Figure 1.** Structural characterization of pristine  $\text{Zn}_{80}\text{Cu}_{20}$  alloy ribbons prepared by melt spinning. (a) SEM micrograph at a scale bar of  $1\ \mu\text{m}$ ; inset: photograph of pristine ribbons. (b) XRD profile with Rietveld analysis signifies the formation of a hexagonal  $\text{Zn}_{80}\text{Cu}_{20}$  crystal phase with space group of  $P6_3/mmc$ , lattice parameter of  $a = 2.734 \pm 0.001\ \text{\AA}$  and  $c = 4.293 \pm 0.001\ \text{\AA}$ , and crystallite size of  $165 \pm 4\ \text{nm}$ . Difference profile is denoted in grey line. The  $R_{\text{wp}}$  is the  $R$ -weighted pattern as a quality of the fit. Blue hollow circles denote the  $\text{Zn}_{80}\text{Cu}_{20}$  reference pattern (ID: #1524894 from COD<sup>41</sup>). (c) XPS Auger spectra and the corresponding fit of Zn LMM from the ribbon surface. (d) XPS sputter depth profile up to 77 nm, showing the chemical distribution of Zn. The relatively large error bars are due to the inhomogeneous sputter process.

tion. A dispersion of dealloyed sample in propan-2-ol was pipetted on a holey carbon film-coated TEM grid (EMS, 300 mesh) and dried in air at room temperature. EDX elemental mappings of sample areas of up to  $1\ \mu\text{m}^2$  were performed and evaluated using INCA 5.03 software (Oxford Instruments).

**2.5. X-Ray Diffraction.** To analyze the crystallinity and crystal phases of the pristine and dealloyed ribbons, an X-ray diffractometer Empyrean (PANalytical) equipped with a Cu tube, Bragg–Brentano unit, Soller, and PIXcel<sup>1D</sup> detector was employed. The setting parameters were as follows:  $2\theta$  range from  $10$  to  $90^\circ$ , step size of  $0.03^\circ$ , counting time of  $900\ \text{s}$ , sample spinning time of  $2\ \text{s}$ , and total acquisition time of  $3\ \text{h}$ . Data processing and evaluation were performed using TOPAS 5 software and HighScore 4.5 software.

**2.6. X-Ray Photoelectron Spectroscopy.** The surface composition and chemical state of Zn and Cu species in the pristine and dealloyed ribbons were characterized using an ESCALAB 250 Xi spectrometer (Thermo Fisher). The X-ray photoelectron spectroscopy (XPS) spectra were collected with monochromatic Al  $K\alpha$  radiation with a photon energy of  $1486.6\ \text{eV}$ . Survey spectra were collected from  $0$  to  $1350\ \text{eV}$  with pass energy of  $100\ \text{eV}$  and resolution step of  $1\ \text{eV}$ . Experimental parameters for the acquisition of high resolution XPS spectra of C  $1s$ , O  $1s$ , Cu  $2p$ , and Zn  $2p$  as well as Auger spectra of Cu and Zn LMM are summarized in Table S1 of the Supporting Information. An Ar ion source (MAGCIS, Thermo Fisher) was used to sputter a geometric area of approximately  $2.25\ \text{mm}^2$ . For XPS measurements and sputter processes, we

introduce the samples shortly and did not heat them to avoid any contamination. A sequence of depth profile measurements consisted of 3 sputter cycles at  $2\ \text{kV}$  for  $30\ \text{s}$ , followed by 5 sputter cycles at  $4\ \text{keV}$  for  $120\ \text{s}$ , and finally one cycle at  $4\ \text{keV}$  for  $300\ \text{s}$ . Local temperature increase on the sputtered area of the samples under vacuum accelerated the volatilization rate of Zn based on the differences in temperature dependence of the saturated vapor pressures of zinc and copper.<sup>38–40</sup> For this reason, results from the elemental XPS depth profiles of pristine ribbons were corrected by the standard deviations calculated from a commercial ZnCu alloy (Alfa Aesar, brass foil alloy 260, Cu 69%, Zn 31%) shown in Figure S1, where experimental composition shows  $84.3$  and  $15.7\ \text{at.}\ \%$  Cu and Zn, respectively. Data analysis was performed by Avantage software (Thermo Fisher Scientific, version 5.9911).

### 3. RESULTS

**3.1. Characterization of Pristine  $\text{Zn}_{80}\text{Cu}_{20}$  Alloy Ribbons.** The morphology, crystal structure, and chemical composition of initial  $\text{Zn}_{80}\text{Cu}_{20}$  ribbons prepared by melt spinning were investigated by using SEM, EDX, X-ray diffraction (XRD), and XPS techniques. Figure 1a displays a SEM micrograph of as-prepared ribbons with visible grain boundaries. The dots that appear on the ribbon surface are expected to be oxide species, immediately forming on the metal surface by exposure to air. From the EDX data, the elemental quantification was found to be  $23 \pm 1\ \text{at.}\ \%$  Cu and  $77 \pm 1\ \text{at.}\ \%$  Zn on the surface as well as in the cross-section of

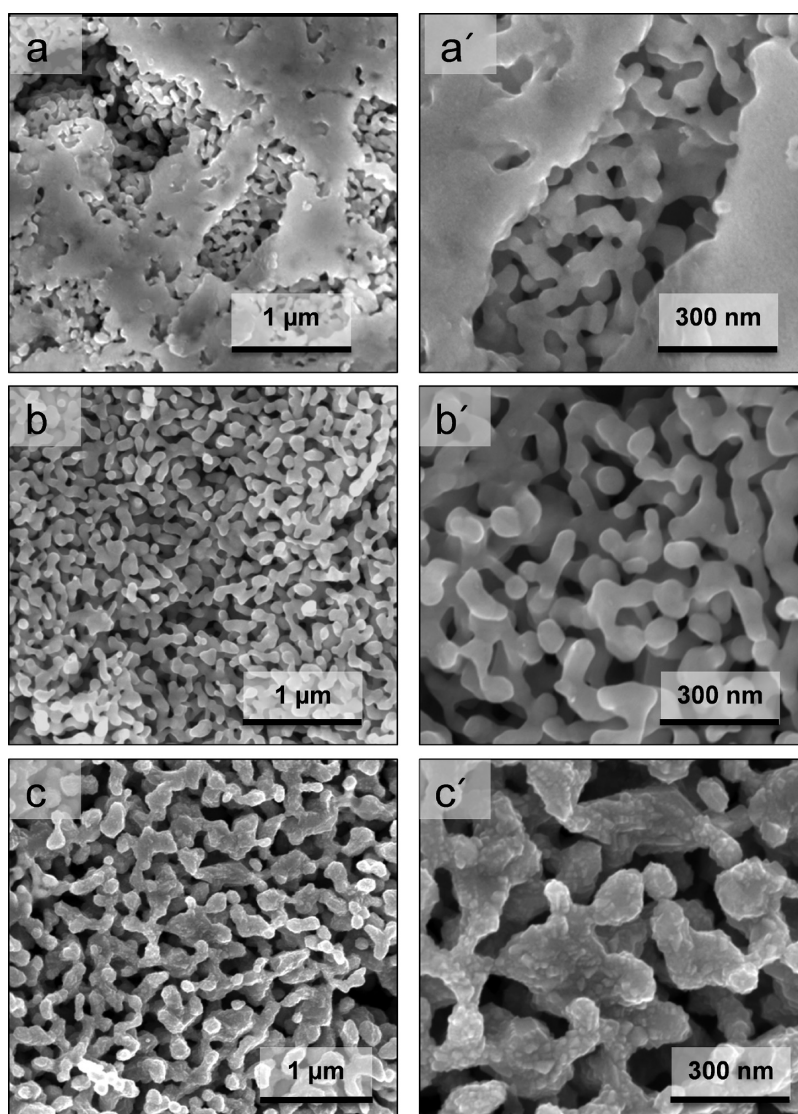


**Figure 2.** Series of low (top) and high (bottom) magnification SEM micrographs of  $\text{Zn}_{80}\text{Cu}_{20}$  ribbons (a,a') after 3.5, (b,b') 24, and (c,c') 312 h (13 days) of dealloying time in 0.1 M HCl at 25 °C under Ar atmosphere.

the as-prepared ribbons. This is in excellent agreement with the crystal structure detected by XRD. The XRD profile in Figure 1b shows reflexes at  $2\theta$  values of 38.1, 42.1, 43.7, 58.1, 68.7, 77.9, 83.9, and 84.9°. Rietveld analysis indicated that these reflexes correspond to a hexagonal  $\text{Cu}_{20}\text{Zn}_{80}$  phase with space group of  $P6_3/mmc$  (COD,<sup>41</sup> pattern ID: #1524894). Other crystal phases, for example, monometallic metals or oxides were not detected by XRD.

Moreover, the survey and high resolution XPS spectra of Zn 2p, Cu 2p, and O 1s spectra of the ribbon surface are shown in Figure S2 of the Supporting Information. In Figure S2a,b, the Cu 2p and Zn 2p XPS spectra were deconvoluted and fitted with a doublet for Cu 2p<sub>1/2</sub> and Cu 2p<sub>3/2</sub> at 953.2 and 933.3 eV as well as for Zn 2p<sub>1/3</sub> and 2p<sub>3/2</sub> at 1045.5 and 1022.1 eV, respectively. The low intensity of the Cu 2p data signifies its minor content on the ribbon surface. To identify the chemical state of Zn, we also analyzed the corresponding Zn Auger spectra (Figure 1c), signifying three different oxidation states, namely for metallic Zn (blue line, at 491.4 and 494.7 eV),<sup>42</sup> for ZnO (green line, at 496.2 and 498.5 eV)<sup>42</sup> and finally for Zn(OH)<sub>2</sub> species (red line, at 499.8 eV).<sup>43</sup> The formation of

metal oxide and hydroxide species is confirmed by the O 1s XPS spectrum (peak maxima at 530.9 and 532.5 eV), as shown in Figure S2c. The results from the deconvoluted XPS spectra clearly reveal that the top layer of  $\text{Zn}_{80}\text{Cu}_{20}$  alloy ribbons is Zn-enriched and strongly oxidizes, forming a passivation layer with a thickness of few nanometers. The segregation of Zn to the surface is likely related to melt spinning process and/or its strong oxophilic character, when ribbons are in contact with air. Very likely, during the melt-spinning the liquid ZnCu impinges a rotating cooled wheel. This quenching might lead to a change in mobility of Cu and Zn atoms based on the different melting temperatures. In other words, zinc shows a lower melting temperature and is therefore more mobile compared to copper with higher melting temperature. Thus, starting from the precipitation of denser ZnCu liquid, Zn atoms tend to segregate to the surface during the quenching process.

In Figure 1d, the XPS sputter depth profile of pristine  $\text{Zn}_{80}\text{Cu}_{20}$  ribbons shows the chemical distribution of Zn and Cu up to 77 nm of depth. After the first few mild sputter cycles, the amount of overall oxygen was negligible and only

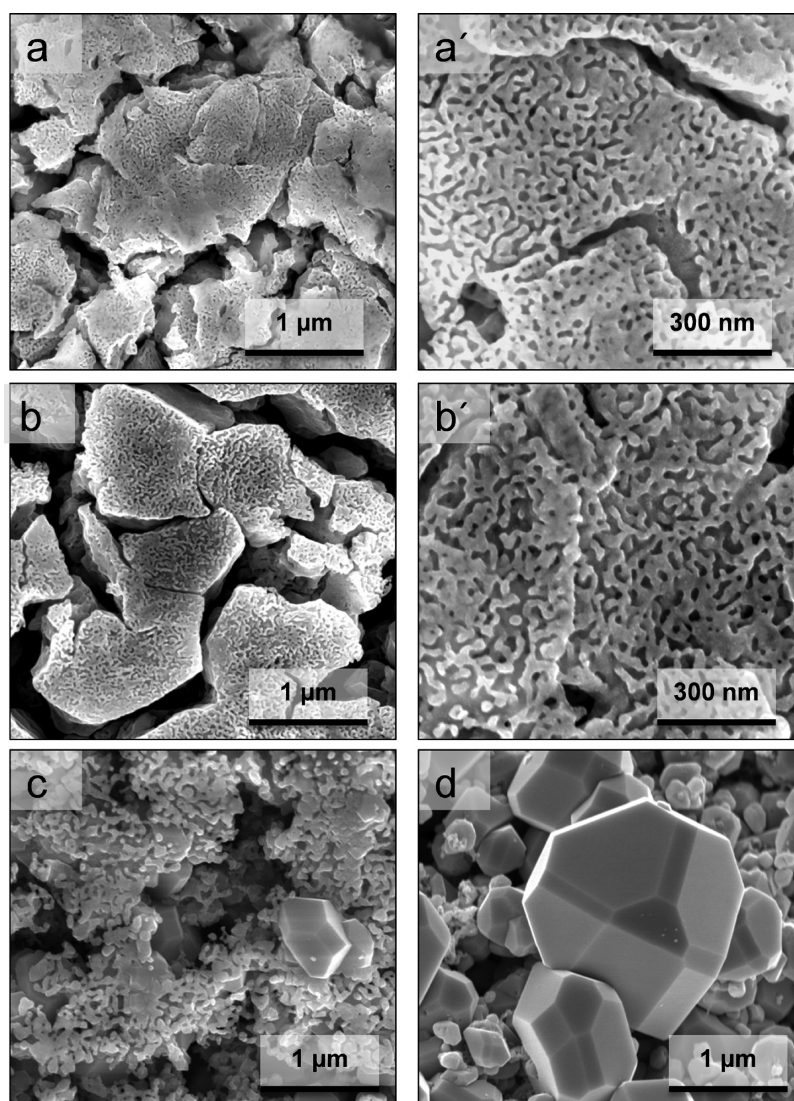


**Figure 3.** Series of low (top) and high (bottom) magnification SEM micrographs of  $\text{Zn}_{80}\text{Cu}_{20}$  ribbons after dealloying time of (a,a') 8, (b,b') 24, (c) 92, and (d) 312 h (13 days) in 1.3 M NaOH at 25 °C under Ar atmosphere.

the ribbon surface is oxidized. Thus, the oxygen content is not illustrated in the depth profile plot. The relatively large error bars represent the deviation of the chemical composition due to the inhomogeneous sputter process of Zn and Cu (temperature dependence of the saturated vapor pressures of zinc and copper).<sup>38–40,44</sup> The apparent composition of the top layers was found to be 93 and 7 at. % for Zn and Cu, respectively. After the first 14 nm depth of the ribbons, the Zn content decreases to  $72 \pm 9$  at. %, while the Cu content simultaneously increases from 7 to  $28 \pm 9$  at. %. Deeper layers up to 77 nm show a relatively constant distribution with  $77 \pm 7$  at. % for Zn and  $23 \pm 7$  at. % for Cu. This result is in excellent agreement with the EDX data.

We can sum up that only the first 14 nm depth of alloy ribbons signifies a Zn-rich surface, but in the deeper layers both metals are homogeneous distributed with an atomic Zn/Cu ratio of 77:23 ( $\pm 7$  at. %).

**3.2. Time-Resolved Ligament Evolution of Dealloyed  $\text{Zn}_{80}\text{Cu}_{20}$  Ribbons.** The effects of nature of electrolyte on the ligament evolution over dealloying time were investigated for pristine  $\text{Zn}_{80}\text{Cu}_{20}$  alloy ribbons using a combination of SEM, (S)TEM, EDX, XRD, and XPS techniques. Thereby, the

ribbons were dealloyed in 0.1 M HCl and 1.3 M NaOH for different reaction times (3.5, 8, 24, 48, 72, 92, 168, and 312 h) under free corrosion. We chose 0.1 M HCl and 1.3 M NaOH as electrolyte solutions to compare our results with previous work on np-Cu films<sup>17</sup> and other research works.<sup>31,45,46</sup> Throughout this paper, we will denote the multiple np-Cu samples dealloyed at different electrolytes for different dealloying times as follows: np-Cu (electrolyte, time).

After dealloying, metallic grey ribbons changed color to brown/black (in NaOH) and brown (in HCl), see Figure S3 of the Supporting Information. The dealloyed ribbons had to be carefully handled due to the brittle nature of the material. Figure 2 displays a series of low and high resolution SEM micrographs of ribbons dealloyed for 3.5, 24, and 312 h in 0.1 M HCl at 25 °C under Ar atmosphere. In the first 3.5 h of dealloying time, the surface of the ribbons is only partially dealloyed accompanied by the evolution of pores, as shown in Figure 2a,a'. The initial dealloying process takes place preferentially at the grain boundaries of the ribbons. It is well-known that grain boundaries contain defects and under-coordinated surface atoms, where the diffusion rate of atoms along the grain boundaries is higher than the high-coordinated

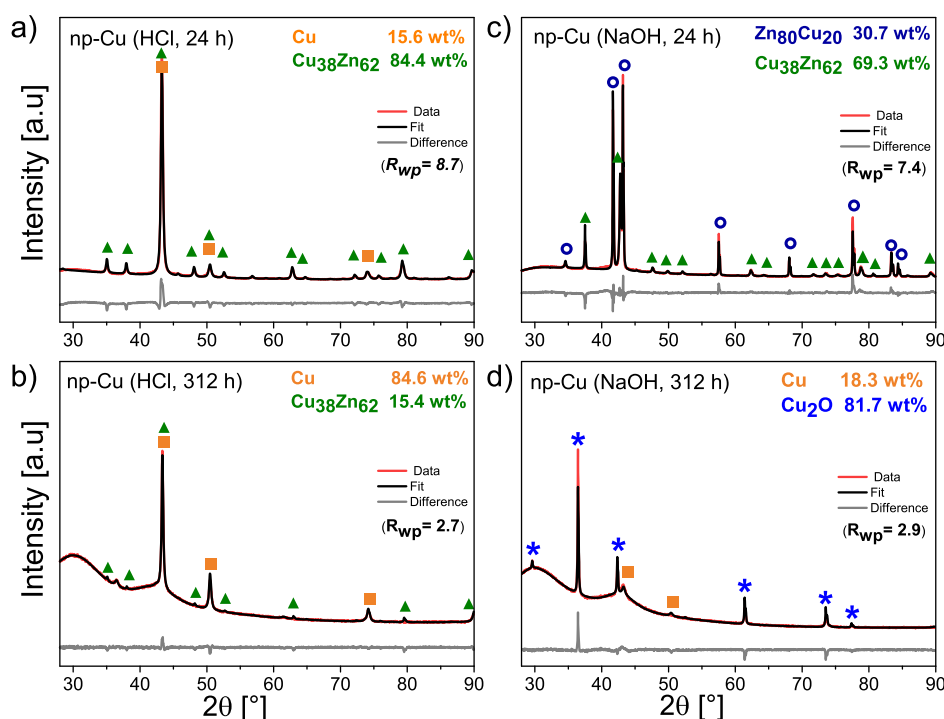


**Figure 4.** XRD profiles for np-Cu materials dealloyed in 0.1 M HCl for (a) 24 and (b) 312 h as well as in 1.3 M NaOH for (c) 24 and (d) 312 h at 25 °C under Ar atmosphere. The wavy background stems from the plexiglass used as a substrate for dealloyed samples. Rietveld analysis: (i) hexagonal  $\text{Cu}_{20}\text{Zn}_{80}$  phase ( $P6_3/mmc$ ),  $a = 2.734 \pm 0.001$  Å,  $c = 4.293 \pm 0.001$  Å, crystallite size of  $165 \pm 4$  nm; (ii) cubic  $\text{Cu}_{38}\text{Zn}_{62}$  phase ( $I\bar{4}3m$ ),  $a = 8.881 \pm 0.002$  Å, crystallite size of  $38 \pm 1$  nm; (iii) fcc Cu phase ( $Fm\bar{3}m$ ),  $a = 3.616 \pm 0.002$  Å, crystallite size of  $29 \pm 3$  nm; (iv)  $\text{Cu}_2\text{O}$  phase ( $Pn\bar{3}m$ ),  $a = 4.269 \pm 0.001$  Å, crystallite size of  $96 \pm 3$  nm. The following reference pattern IDs from the COD<sup>41</sup> were taken: blue hollow circles (ID: #1524894) for  $\text{Zn}_{80}\text{Cu}_{20}$ , green triangles (ID: #1100057) for  $\text{Cu}_{38}\text{Zn}_{62}$ , orange squares (ID: #4105040) for Cu, and blue stars (ID: #1000063) for  $\text{Cu}_2\text{O}$ . Difference profiles are denoted in grey line. The  $R_{wp}$  is the  $R$ -weighted pattern as a quality of the fit.

terrace atoms on the grain surfaces.<sup>47,48</sup> The appearance of pits signifies the attack of aggressive electrolyte at defect-rich parts of the ribbon surface, for example, formed during reduction of the oxide-contained species visible as dots in the SEM micrograph, Figure 1a. Micro-cracks are observed in the dealloyed ribbons due to the strong volume changes during the Zn dissolution and the resulting crystal transformation from hexagonal close packed (hcp) to face-centered cubic (fcc). Over dealloying time, the evolution of pores is more and more pronounced, implying the continuous Zn dissolution from the surface of alloy ribbons. An entire formation of porous network structure, denoted as np-Cu material, is clearly observed after 24 h of dealloying time, displayed in Figure 2b,b'. It is well known that the evolution of pores is controlled by the critical interplay between dissolution rate of less noble metal atoms and surface diffusion rate of remaining noble metal atoms. The np-Cu (HCl, 24 h) consists of self-assembled and homogeneous ligaments. Recently, a loss of ligament structure has been reported for np-Cu films after 72 h of dealloying time in 0.1 M HCl.<sup>17</sup> For this reason, a very long dealloying period was applied to evaluate the structural and chemical stability of the np-Cu materials in HCl. Figure 2c,c' display the low and high resolution SEM micrographs of the np-Cu after dealloying time of 312 h (13 days) in 0.1 M HCl at 25 °C under Ar atmosphere. The np-Cu (HCl, 312 h) shows ligaments with larger size and rough ligament surfaces compared to np-Cu (HCl, 24 h). The visible coarsening of the porous structure can be attributed to the rapid surface diffusion of Cu at the surface–electrolyte interface over time induced by the presence of adsorbed chloride anions and by the tendency

for surface energy reduction.<sup>49,50</sup> This contrary observation can be explained by the different initial thicknesses and homogeneity of pristine  $\text{Zn}_{80}\text{Cu}_{20}$  master alloys used in our previous study. The time-resolved changes in ligament size and chemical composition of np-Cu will be discussed later in more details.

Dealloying of the ribbons in alkaline solution shows a different behavior to that observed in acidic environment. Figure 3 displays a series of low and high resolution SEM micrographs of np-Cu after various dealloying times (8, 24, 92, and 312 h) in 1.3 M NaOH at 25 °C under an Ar atmosphere. Figure 3a,a' shows the increased appearance of micro-cracks, forming along the grain boundaries of  $\text{Zn}_{80}\text{Cu}_{20}$  alloy ribbons after 8 h of dealloying time. Beside the micro-cracks, ligaments with smaller size, and less intense in depth compared to those in np-Cu (HCl) are formed within the grain. It is noted that no ligament formation is observed below a dealloying time of 8 h in NaOH. With increasing dealloying time, the structure and distribution of ligaments in np-Cu (NaOH, 24 h) are similar to those observed after 8 h dealloying time, in Figure 3b,b'. Only the cracks appear much deeper with increasing dealloying time in alkaline media. The extent of the dealloying time up to 92 h leads to larger ligaments with more depth to the porous structure, as shown in the SEM micrograph of the dealloyed ribbons (Figure 3c). Interestingly, octahedral crystals with different sizes appear at the surface of the np-Cu (NaOH, 92 h). Further XRD and XPS analysis could identify the structure and composition of these crystals to be Cu(I)oxide (see Figure 4d). These crystals grew in frequency and size by increasing the dealloying time in alkaline solution. After 312 h (13 days),

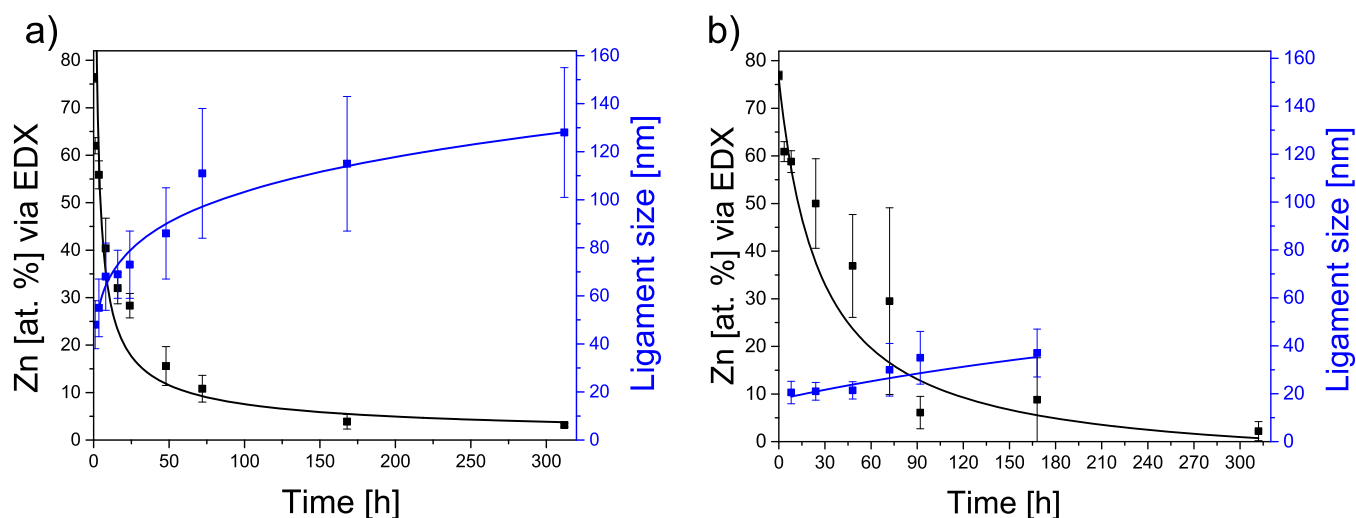


**Figure 5.** Dependence on dealloying time, residual Zn content, and ligament size after chemical dealloying of  $\text{Zn}_{80}\text{Cu}_{20}$  ribbons in (a) 0.1 M HCl and (b) 1.3 M NaOH at 25 °C under Ar atmosphere. The EDX quantification of chemical composition was determined from at least three sample areas at low magnification, while at least 200 ligaments from several SEM micrographs were analyzed to establish the mean ligament size. Each measurement was repeated at least 3 times for each sample.

the surface of the dealloyed ribbons is entirely covered with  $\mu\text{m}$ -sized  $\text{Cu}_2\text{O}$  crystals, as shown in Figure 3d. Based on the SEM analysis, we suggest that the dealloying might be controlled by the propagation of the three-dimensional bicontinuous ligament pore structure and thus the surface diffusion process at the alloy–electrolyte interface. This will be discussed in more details later.

To correlate the morphological alterations from the SEM analysis with the changes in crystallographic phase structure and composition, XRD investigations and quantitative Rietveld analysis on treated ribbons were performed after various dealloying times in HCl and NaOH. In Figure 4a, the XRD profile of the np-Cu (HCl, 24 h) shows  $2\theta$  reflexes at 34.9, 37.9, 43.2, 48.0, 50.5, 52.6, 62.8, 64.7, 72.2, 75.8, 79.2, and 89.6°, ascribing to the cubic  $\text{Cu}_{38}\text{Zn}_{62}$  (COD,<sup>41</sup> reference pattern ID: #1100057) with a space group of  $I\bar{4}3m$ . In fact, the dissolution of zinc is accompanied by the changes in crystal structure from hexagonal  $\text{Cu}_{20}\text{Zn}_{80}$  phase ( $P6_3/mmc$ ) to cubic  $\text{Cu}_{38}\text{Zn}_{62}$  ( $I\bar{4}3m$ ). Additional  $2\theta$  reflexes at 43.3, 50.5, and 74.1° are detected for the np-Cu (HCl, 24 h), corresponding to the fcc Cu phase with  $Fm\bar{3}m$  (COD,<sup>41</sup> pattern ID: 4105040). Quantitative Rietveld refinement indicates  $84.4 \pm 0.9$  and  $15.6 \pm 0.9$  wt % for  $\text{Cu}_{38}\text{Zn}_{62}$  and pure Cu, respectively. The contribution of the pure Cu crystal phase grows by increasing dealloying time, indicating the successive loss of Zn from the bulk ribbons. Finally, after dealloying time of 312 h in HCl (Figure 4b), the Cu amount reaches  $84.6 \pm 1.0$  wt % and the  $\text{Cu}_{38}\text{Zn}_{62}$  phase contributes to only 15.4  $\pm$  1.0 wt %.

In alkaline media, however, the XRD patterns of dealloyed ribbons were found to be strongly different. Two crystal phases,  $\text{Cu}_{20}\text{Zn}_{80}$  and  $\text{Cu}_{38}\text{Zn}_{62}$ , were observed in np-Cu (NaOH, 24 h), shown in Figure 4c, with contribution of  $30.7 \pm 0.5$  and  $69.3 \pm 0.5$  wt %, respectively. The octahedral crystals observed in the SEM micrographs of np-Cu (NaOH, 312 h; Figure 3d) are also confirmed as Cu(I)oxide (COD,<sup>41</sup> ID pattern: 1000063, space group  $Pn\bar{3}m$ ) by XRD. The  $\text{Cu}_2\text{O}$  phase is represented by  $2\theta$  reflexes at 29.5, 36.4, 42.3, 61.4, 73.5, and 77.4°. Quantitative Rietveld analysis reveals  $81.7 \pm 3.4$  and  $18.3 \pm 3.4$  wt % for  $\text{Cu}_2\text{O}$  and Cu, respectively. The

wavy background in the XRD profiles is caused by the plexiglass used as sample holder (see Figure S4) due to the low sample quantities available for these measurements.

In Figure 5, the compositional changes obtained from EDX are correlated with the dealloying time in HCl and NaOH. It also shows the trend, by which the ligament size alters with respect to the Zn content and dealloying time. First, we will describe the loss of Zn as a function of the dealloying time in 0.1 M HCl (Figure 5a). As the dealloying rate is associated with the dissolution rate of less noble metal from master alloy, it is obvious that the Zn content continuously decreases in HCl over time. The dissolution rate of Zn from the ribbon surface is very fast in the first hours of dealloying process. Within the first 3.5 h of dealloying time, the Zn content drops drastically from  $77 \pm 1$  at. % (pristine) to  $56 \pm 3$  at. %. After 24 h dealloying time, the remaining Zn content is  $32 \pm 5$  at. % and continues to decline to  $16 \pm 4$  at. % after 48 h. Finally, the Zn content was found to be  $3 \pm 2$  at. % after 168 h and it remains almost constant until 312 h of dealloying time. The corresponding SEM micrographs of np-Cu (Figure 2c,c') reveals that 2–3 at. % of Zn is still sufficient to retain the ligament structure. An entire loss of zinc leads to a loss of ligament structure and results in a polycrystalline solid film.<sup>17</sup>

In Figure 5b, the dealloying of ribbons in 1.3 M NaOH shows a decrease in Zn content over time. At the beginning, the residual Zn content for np-Cu (NaOH, 3.5 h) was found to be similar to np-Cu (HCl, 3.5 h) with amount of 55–60 at. %. After that, the process became much slower in alkaline media. The amount of residual Zn dropped to  $50 \pm 9$  at. % after 24 h, and  $37 \pm 11$  at. % after 48 h, until it had reached 1–2 at. % after 312 h (13 days). An important finding to notice in alkaline medium is the detection of large amount of oxygen that increases strongly from  $24 \pm 10$  at. % (after 92 h) to  $45 \pm 19$  at. % (after 312 h). The correlation of O, Cu and Zn contents over dealloying time in NaOH is shown in Figure S5 of the Supporting Information. As the atomic Cu/O ratios obtained over time deviate from  $\text{Cu}_2\text{O}$ , we suggest that the formation of Zn and Cu (hydr)oxide surface species occurs during the dealloying process in an alkaline corrosive environment.

It is also important to clarify how the ligament size in the np-Cu materials changes over dealloying time in HCl and NaOH at 25 °C. The mean ligament size was determined by analyzing of at least 200 ligaments from several SEM micrographs. Figure S5a displays the changes in ligament size as a function of dealloying time in 0.1 M HCl. In fact, the formed ligaments of np-Cu materials become larger and rougher over dealloying time. More precisely, the mean ligament size increases from  $55 \pm 12$  nm (3.5 h) to  $73 \pm 14$  nm (24 h) and finally to  $128 \pm 27$  nm (312 h) in HCl. Due to coarsening of the ligaments in contact with a strong acid, the size distribution becomes broader as illustrated in Figure S6 of the Supporting Information. In this context, the residual Zn content decreases concurrently from  $56 \pm 3$  to  $32 \pm 5$  at. % and finally to  $3 \pm 1$  at. %. Thus, a reverse correlation is observed between the ligament size and residual Zn content in np-Cu by dealloying in HCl.

Contrary to the dealloying behavior in acid, the ligament size of np-Cu remains almost unchanged with a size of  $21 \pm 4$  nm until 48 h of dealloying time in 1.3 M NaOH, see Figure 5b. It is noted that the ligament size distributions are very narrow (see Figure S7). After that, a slight increase of the mean ligament size up to  $36 \pm 11$  nm (1.7 fold) is observed. Obviously, the ligament size formed during dealloying in NaOH is much smaller than those in HCl.

Due to its very high solubility in HCl as well as NaOH, we suggest that a supersaturation of soluble Zn compounds, for example,  $\text{ZnCl}_2$  or  $\text{Zn}(\text{OH})_4^{2-}$ , might not be reached in these electrolyte solutions, because no precipitation of Zn salts and no alteration of surface diffusion rate at the alloy–electrolyte interface have been observed. As shown in Figure 3d, only large Cu(I)oxide crystals via continuous re-deposition form and mainly cover the entire surface after 312 h of dealloying time in 1.3 M NaOH. We can sum up that the ligament size is independent from residual Zn content in the first 48 h of dealloying in alkaline media because of the lower diffusivity of Cu atoms by forming hydr(oxide) species along the alloy–electrolyte interface. This information is particularly useful for systematic studies of np-Cu materials in heterogeneous and electrochemical catalysis.

We wanted to mention that in all experiments a Cu substrate was attached to the pristine  $\text{Zn}_{80}\text{Cu}_{20}$  ribbons during dealloying in 1.3 M NaOH. This was found to be essential for initiating and accelerating the dealloying process on Zn-rich surface. The high overpotential of the cathodic hydrogen evolution reaction (HER) as an opposite reaction hinders the oxidative dissolution of Zn and thus slows down the dealloying process by passivation. More precisely, the residual Zn content of dealloyed ribbons in 1.3 M NaOH for 312 h (13 days) was found to be  $62 \pm 2$  at. % (SEM micrographs, Figure S8). When the ribbons, however, were attached to a Cu substrate, the Zn dissolution process was enhanced and dropped to  $61 \pm 2$  at. % after only 3.5 h of dealloying time. The *iR*-corrected HER polarization curves for pristine  $\text{Zn}_{80}\text{Cu}_{20}$  ribbons and monometallic compounds are displayed in Figure S9, signifying a decrease of the overpotential for HER in the order of: pure Cu <  $\text{Zn}_{80}\text{Cu}_{20}$  < pure Zn in 1.3 M NaOH. Thus, the passivation layer of a Zn-rich ribbon surface can break down in strong alkaline environment, when an electrochemical cathodic reaction like HER on more active metal surface with lower activation barrier (overpotential) is offered. This is also visible by the hydrogen bubble formation on the attached Cu foil, but not on the ribbons alone (Figure S10).

### 3.3. Effects of Dealloying Temperature, Electrolyte Agitation, and De-aeration on the Structure of np-Cu.

The effect of electrolyte agitation on the pore-ligament evolution of np-Cu ribbons during the first 24 h of dealloying in de-aerated 0.1 M HCl at room temperature was studied to point out any mass transport restrictions based on the electrolyte solution within the pores. Figure S11 summarizes the results from the dealloyed samples with and without agitation evaluated by SEM–EDX measurements in the top and cross-sectional view. A similar dealloying behavior is observed in stagnant and agitated HCl solutions. The chemical composition, ligament size as well as the dealloying depth over the first 24 h (see Figure S11c) are very similar with and without stirring. A slight difference of the residual Zn content was observed after dealloying of more than 8 h. We explained this observation by the different formation of laminar film resistance on the ribbon surface with and without convection as mass transport resistance.

The effect of de-aeration of the electrolyte was also investigated in HCl. Figure S12 and Table S2 in the Supporting Information show very similar results of the np-Cu ribbons in aerated and de-aerated 0.1 M HCl at room temperature. We can point out that the de-aeration of HCl solution has no influence on microstructure evolution characteristics of np-Cu ribbons during dealloying. However, the de-aeration of aggressive electrolyte solution is important when the dealloying takes place in alkaline media, where soluble zinc species reacts with carbon dioxide from the air to form zinc carbonate. Zinc carbonate is insoluble in water, thus it precipitates on the surface of the ribbons and terminates the dealloying process.

The dealloying temperature is very important parameter that influences the structure of np-Cu. Thus, the  $\text{Zn}_{80}\text{Cu}_{20}$  ribbons were dealloyed for 24 h in 0.1 M HCl at 15, 25 and 50 °C. Figure S13a,b in the Supporting Information display the changes in residual Zn content and ligaments size with the dealloying temperature. The EDX analysis shows Zn content of  $17 \pm 3$  at. % at 50 °C, compared to  $32 \pm 5$  at. % at 25 °C. The mean ligament size increases with higher dealloying temperature from  $64 \pm 12$ , to  $73 \pm 14$  to  $84 \pm 15$  nm at 15, 25 and 50 °C, respectively. The observed ligament size growth is related to the temperature-dependent surface diffusion rates of Cu atoms, as reported in the literature.<sup>51–53</sup> Surface diffusivity of Cu along the alloy–electrolyte interface ( $D_s$ ) is estimated from the following equation<sup>52–58</sup>

$$D_s = \frac{d(t)^4 KT}{32\gamma\alpha^4} \quad (1)$$

where  $d(t)$  in [m] is the ligament size at given dealloying time  $t$ ,  $K$  is the Boltzmann constant ( $1.3806 \times 10^{-23}$  J K<sup>-1</sup>),  $T$  in [K] is the dealloying temperature,  $\gamma$  is the surface energy of Cu ( $1.79$  J m<sup>-2</sup>),<sup>52,54,57</sup>  $t$  in [s] is the dealloying time, and  $\alpha$  is the lattice parameter of Cu ( $3.616 \times 10^{-10}$  m). The calculated  $D_s$  values of Cu in 0.1 M HCl were found to be  $7.9 \times 10^{-19}$ ,  $1.4 \times 10^{-18}$  and  $2.6 \times 10^{-18}$  m<sup>2</sup> s<sup>-1</sup> at 15, 25 and 50 °C, respectively. Our results are in good agreement with the reported values from Aburada et al.<sup>55</sup> in HCl and Erlebacher<sup>59</sup> in vacuum.

Because the nanostructure is dependent on the dealloying time and temperature, measurement of the activation energy ( $E_a$ ) is necessary to better understand the dealloying mechanism. An Arrhenius plot in Figure S13c shows a linear relationship between  $\ln D_s$  and  $1000/T$  based on our



experimental data. The slope of the fitted line equals to  $-E_a/R$ , where  $R$  is the gas constant ( $8.3145 \text{ J mol}^{-1} \text{ K}^{-1}$ ).<sup>52,56</sup> In this work,  $E_a$  was determined to be  $25.8 \text{ kJ mol}^{-1}$ . Zhang et al.<sup>58</sup> have reported an  $E_a$  value of  $36.6 \text{ kJ mol}^{-1}$  for Cu in 0.1 M HCl, which is comparable to our result.  $E_a$  values between 17 and  $62 \text{ kJ mol}^{-1}$  were reported in NaOH,  $\text{H}_2\text{SO}_4$  and HF solutions.<sup>51,52,56,58</sup>

Based on our experimental data, the surface diffusivity of Cu in 1.3 M NaOH at  $25^\circ\text{C}$  was estimated to be  $9.4 \times 10^{-21} \text{ m}^2 \text{ s}^{-1}$ , which is three orders slower than the diffusivity in 0.1 M HCl at  $25^\circ\text{C}$  ( $1.4 \times 10^{-18} \text{ m}^2 \text{ s}^{-1}$ ). Therefore, smaller ligament sizes in alkaline media are attributed to the slower surface mobility of Cu atoms along the alloy–electrolyte interface. This allows controlling the Zn content from  $59 \pm 3 \text{ at. \%}$  (NaOH, 8 h) to  $37 \pm 11 \text{ at. \%}$  (NaOH, 48 h) independent from the ligament size. Very interestingly, the ligament size could not be increased by simply adding NaCl into 1.3 M NaOH. An opposite trend is even observed, so that the ligament size becomes smaller. This observation is not yet fully understood and further investigations are required. We can sum up that the nature of electrolyte and dealloying temperature have a strong influence on the surface diffusion of Cu atoms and hence on microstructure evolution characteristics of np-materials.

**3.4. Spatial Distribution of Residual Zn Atoms in the Ligaments.** Further investigations of the spatial distribution of residual Zn atoms within the ligaments of np-Cu were verified using the high-resolution STEM–EDX technique. EDX mappings of Cu (red) and Zn (green) within a single ligament of np-Cu ribbon (HCl, 168 h) are displayed in Figure 6. The average Zn content of the entire ligament (Figure 6a) was found to be 3 at. %, which is in excellent agreement with the SEM–EDX analysis in Figure 5. Very interestingly, the overlaid EDX mapping (Figure 6b) clearly shows a Zn enrichment up to ca. 12 at. % in these regions, while Zn-poor regions only contain 1–2 at. %. Separate EDX mappings of Cu and Zn are also shown in Figure 6c,d, respectively. This heterogeneous distribution of the less noble metal has recently been reported in np-Au showing Ag rich domains within the ligaments.<sup>60,61</sup> The formation of Ag-rich regions is very likely related to the critical interplay between the Ag dissolution rates and the remaining Au surface diffusion rates. The remaining Au surface atoms might trap the near-surface Ag atoms and prevent their exposure to the corrosive electrolyte for dissolution. This trapping of Zn atoms near the surface by passivation of more noble Cu surface atoms might explain the appearance of Zn-rich regions inside the np-Cu ribbons. Thus, we suggest that the residual Zn atoms are located in the relics of the master alloy. Obviously, the average concentration of Zn in the whole ligament is only an approximation, obtained from the bulk EDX, as the local Zn concentration differs within the ligaments. To sum up, the distribution of Zn atoms inside the ligaments of np-Cu materials is heterogeneous and, as a consequence, the appearance of Zn-rich regions near the surface might influence their catalytic properties, for example, for electrochemical  $\text{CO}_2$  reduction reaction.

**3.5. Cross-Section Analysis of np-Cu Ribbons.** Until now, the porosity of np-Cu ribbons was analyzed by SEM from the plane view (see Figures 2 and 3). To evaluate the dealloying front propagation within the relatively thick ribbons, cross-sectional SEM–EDX analysis of np-Cu ribbons treated at various dealloying times at constant temperature ( $25^\circ\text{C}$ ) were performed.

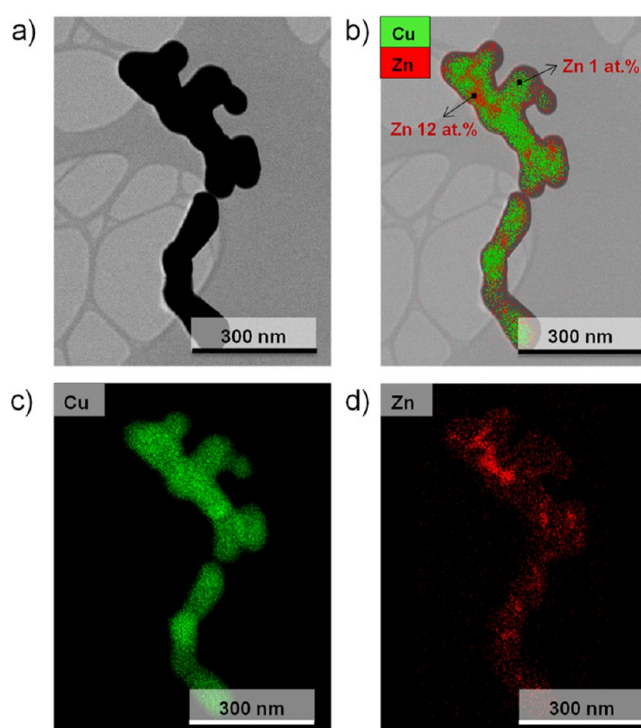


**Figure 6.** Elemental EDX mappings of Zn and Cu atoms inside single ligaments of np-Cu ribbons (HCl, 168 h) probed by STEM–EDX. (a) Bright-field STEM micrograph of single ligaments prepared by dispersion of the np-Cu (HCl, 168 h) in propan-2-ol; (b) overlaid EDX mapping of Cu (in green) and Zn (in red) of the respective sample area, showing Zn-rich and Zn-poor regions; separate EDX mappings of Cu (c) and Zn (d).

Figure 7 displays the cross-sectional SEM micrographs of a selection of np-Cu after dealloying for 24 and 168 h in HCl and for 24 h in NaOH. As an overview, Table 1 lists the comparison between the obtained chemical compositions and ligament sizes of np-Cu in the plane and cross-sectional view of the SEM–EDX measurements. In Figure 7a,a', the cross-sectional SEM micrographs of the np-Cu (HCl, 24 h) show a homogeneous porous microstructure near the surface (comparable to the SEM micrographs in the plane view, Figure 2b,b'), while the inner part is partially solid and dense. Interestingly, the ligaments formed near the surface were found to be smaller with higher Zn content compared to those on the surface. In the cross-sectional and plane view, the mean ligament size and the Zn content for np-Cu (HCl, 24 h) are  $56 \pm 15 \text{ nm}$  at  $52 \pm 6 \text{ at. \%}$  and  $73 \pm 14 \text{ nm}$  at  $32 \pm 5 \text{ at. \%}$ , respectively. It is noted that the residual Zn content and ligament size measured in the inner part of dealloyed ribbons correspond to the surface composition and ligament size of np-Cu (HCl, 3.5 h). Altogether, we can distinguish three regions for the np-Cu (HCl, 24 h).

*Region I:* The surface of the dealloyed ribbons is exposed to the electrolyte all the time and thus commences to coarsen within the first 24 h, resulting in larger ligament size and lower residual Zn content.

*Region II:* Microstructure with smaller ligament size and higher Zn content form near the surface of dealloyed ribbons based on the dealloying front propagation within the master alloy ribbons and less exposure time to the highly aggressive electrolyte.

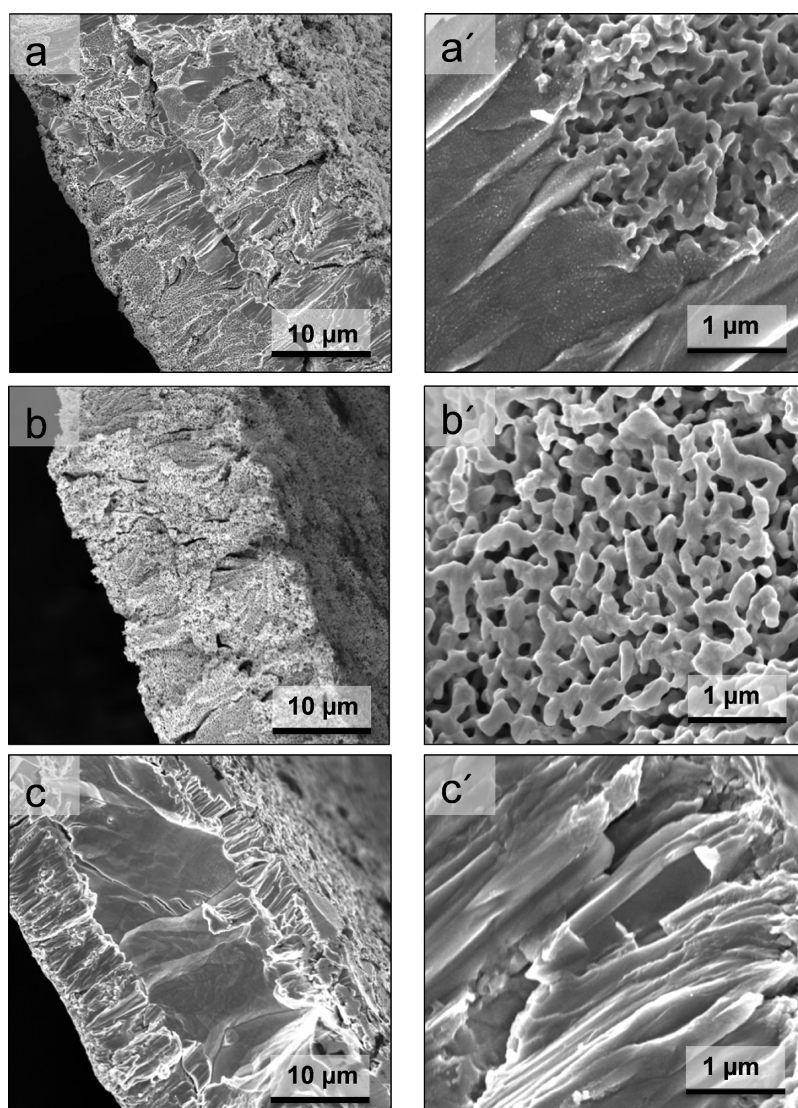


**Figure 7.** Low (top) and high (bottom) magnification cross-sectional SEM micrographs of  $Zn_{80}Cu_{20}$  ribbons dealloyed in (a,a') for 24 and (b,b') 168 h (7 days) in 0.1 M HCl or (c,c') for 24 h in 1.3 M NaOH, respectively.

**Table 1. Comparison of Chemical Composition and Ligament Size between the Surface and Cross-Section of Dealloyed Ribbons**

ribbons	Zn [at. %] <i>via</i> EDX		Cu [at. %] <i>via</i> EDX		ligament size [nm]	
	in plane	cross-sectional	in plane	cross-sectional	in plane	cross-sectional
$Zn_{80}Cu_{20}$ alloy	$77 \pm 1$	$78 \pm 1$	$23 \pm 1$	$22 \pm 1$		
np-Cu (NaOH, 24 h)	$73 \pm 3$	$57 \pm 9$	$78 \pm 3$	$44 \pm 9$	$21 \pm 4$	
np-Cu (HCl, 24 h)	$32 \pm 5$	$52 \pm 6$	$68 \pm 5$	$48 \pm 6$	$73 \pm 14$	$56 \pm 15$
np-Cu (HCl, 168 h)	$3 \pm 2$	$3 \pm 1$	$97 \pm 2$	$97 \pm 1$	$115 \pm 28$	$97 \pm 16$

*Region III:* The center of the master alloy showing dense and solid structure is further unaffected from any dealloying process under free corrosion. Thus, the middle part of the dealloyed ribbons signifies the same composition like the starting alloy ribbons.

With increasing dealloying time, for example, for 168 h = 7 days, we observed a homogenous pore network in the cross-sectional SEM micrograph of dealloyed ribbons, as shown in Figure 7b,b'. The composition of the np-Cu (HCl, 168 h) in the plane and cross-sectional view was found to be very similar (around  $3 \pm 1$  at. %), while the mean ligament sizes is a bit smaller, yet, not very different taking the error bars into

account. Therefore, dealloying for longer period enables to form porous network structure that is controlled by varying the nature of electrolyte solution, pH value, dealloying time, and temperature.

To have a better understanding of the microstructure evolution characteristics and dealloying front propagation of  $Zn_{80}Cu_{20}$  master alloy ribbons during dealloying process in 0.1 M HCl, the dealloying depth during the first 24 h was investigated. It is noted that the total thickness of the ribbons is decreasing during dealloying due to the shrinkage associated with dissolution of large amounts of Zn and phase transformation from hexagonal to cubic structure. More precisely,

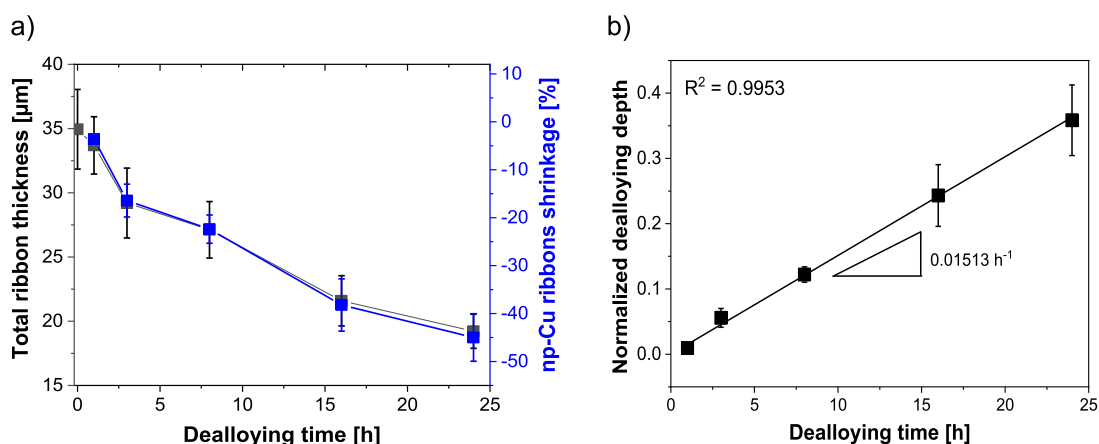


**Figure 8.** Shrinkage of ribbons during dealloying and the dealloying rate. (a) Plot of total ribbons thickness at a given time [ $D_t$ ] in black squares, and np-Cu ribbons shrinkage in thickness [ $100 \times \Delta D/D_0$ ] in blue vs dealloying time in 0.1 M HCl at 25 °C under Ar atmosphere.  $D_0$  is the thickness of the ZnCu alloy ribbons before dealloying, and the change of thickness was calculated by  $\Delta D = D_t - D_0$ . (b) Plot of normalized dealloying depth vs dealloying time in 0.1 M HCl at room temperature under Ar atmosphere. The normalized dealloying depth was calculated from the ratio of the dealloying depth and the ribbon thickness at a given time ( $D_t$ ). Each measurement was repeated 3 times for each sample.

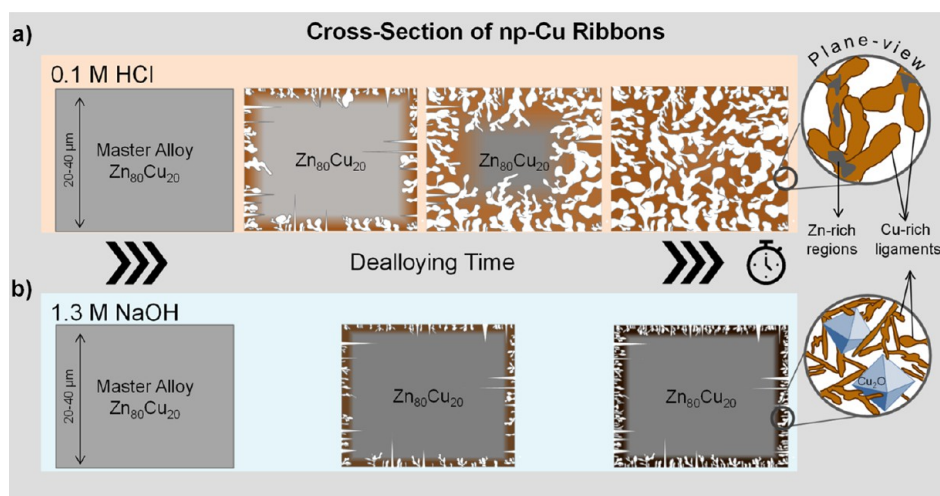


**Figure 9.** Schematic of the dealloying front propagation for the pore-ligament evolution of np-Cu ribbons. (a) Dealloying in 0.1 M HCl; the first graph represents a cross-section of Zn<sub>80</sub>Cu<sub>20</sub> alloy and the next graph displays the formation of cracks and the evolution of ligament on the surface of the ribbons, the following graphs show the dealloying front propagation during the dealloying time. The zoomed graph on the top right represents the plane-view ligaments with Zn-rich regions inside the ligaments. (b) Dealloying in 1.3 M NaOH: over time, ligaments form only on the surface and do not grow into deeper level of the ribbons. The zoomed graph on bottom right shows the plane-view ligaments with octahedral Cu(I)oxide crystals. The master alloy is denoted in grey color, Zn-rich regions in dark-gray, Cu-rich ligaments in brown in acidic media, and in brown/black in alkaline media.

the total thickness strongly decreased about 45%, from  $35 \pm 3$  to  $19 \pm 1$  μm, after 24 h of dealloying (see Figure 8a). Figure 8b Such a strong shrinkage has been reported for np-Co, where cross-section thickness is decreased by 55% after dealloying.<sup>44</sup> To consider the strong shrinkage of the ribbons, the dealloying depth was normalized by dividing its value by the total thickness of the ribbons at each dealloying time. In Figure 8b shows a plot of normalized dealloying depth versus dealloying time. We observed a linear relationship between normalized dealloying depth and dealloying time, indicating that the rate of dealloying front propagation is constant. This suggests that the dealloying is controlled by the interfacial processes.<sup>12,53,62–64</sup> If the mass transport of the electrolyte (diffusion of corrosive electrolyte solution in and out of the porous layers) would be the rate-limiting step, we would have seen slower dealloying front propagation over the dealloying period. Therefore, we conclude that the microstructure of np-

Cu is controlled by the interfacial process, which is occurring at the interface between the alloy and electrolyte.

Based on the plane-view SEM micrographs in Figure 3, we assumed that the ligaments mainly form at and near the surface of the ribbons dealloyed for 24 h in 1.3 M NaOH. The cross-sectional SEM–EDX analysis (Figure 7c,c' and Table 1) confirms our observation. Only the surface of the ribbons which is directly exposed to NaOH shows a porous microstructure, while the inner part is still dense and solid. For the np-Cu (NaOH, 24 h), the content of Zn was found to be  $73 \pm 3$  and  $57 \pm 9$  at. % near the surface (cross-section) and on the surface (in plane), respectively. The solid and dense inner part of the ribbon is very similar in morphology and chemical composition to the starting one (see cross-sectional SEM micrograph of pristine Zn<sub>80</sub>Cu<sub>20</sub> ribbons in Figure S13). We can sum up that the dealloying process and thus the pore evolution are much slower in alkaline media compared to those

in acidic. Since dealloying is an interface-controlled process, Zn dissolution and pore evolution rate control the penetration of the electrolyte and thus the dealloying of the bulk of the ribbons. The small pore network is related to the slower surface diffusion rates of the remaining Cu atoms by forming surface (hydr)oxide, which will be discussed in the next section.

#### 4. DISCUSSION

Starting from  $Zn_{80}Cu_{20}$  alloy ribbons prepared by melt-spinning, the microstructure evolution characteristics of the np-Cu with highly open and three-dimensional pore network is visualized in Figure 9. When the ribbons are immersed in 0.1 M HCl solution, the dealloying process is rapidly initiated by dissolution of Zn atoms from the top Zn-rich surface layer of alloy ribbons. This process leaves the more noble Cu surface atoms unstable and highly low-coordinated. The remaining Cu surface atoms tend to diffuse along the top layers and additional Zn atoms within the near-surface layers are successively exposed to the aggressive electrolyte. Therefore, a critical interplay between Zn dissolution rates and surface diffusion rates of Cu atoms controls the formation of highly porous and well-connected ligament network.

Dealloying is controlled by the interfacial processes mentioned above. In case of using chloride-containing acidic solution, the chloride ions enhance the mobility of Cu surface atoms by 2–5 magnitudes compared to a chloride-free environment.<sup>16,37</sup> Chloride ions can adsorb on a Cu-based surface, especially at low-coordinated sites and increase its mobility.<sup>37,49</sup> This leads to formation of larger ligaments and pores. The addition of chloride ions to an alkaline solution showed an opposite effect, which is still not well understood to date. Surface diffusion rate is also strongly affected by the dealloying temperature. The increased diffusivity of Cu with higher temperature leads to enhanced coarsening and larger ligament size. On the other hand, agitation of the electrolyte during dealloying does not have a significant influence on the structure because the mass transport of electrolyte into the pores is not the rate-limiting step in the dealloying process. The obtained ligament sizes in this work are in good agreement with the results published from other groups.<sup>16,31,33,36,49,65</sup> An overview about the structural information and its experimental conditions for the formation of np-Cu are listed in Table S3 of the Supporting Information. The enhanced Cu surface diffusion in HCl allows the dealloying front propagation into the entire ribbons (initial thickness of ribbons of  $35 \pm 3 \mu\text{m}$ ). Therefore, dealloying in HCl solution allows for the formation of homogeneous np-Cu-rich materials.

Apart from the degree of porosity, we investigated the spatial distribution of Zn atoms within the np-Cu. Very interestingly, some Zn atoms could be trapped in the Cu-rich clusters and are not exposed to the aggressive electrolyte. This results in Zn-enriched regions within the ligaments of np-Cu, which is very likely caused by the surface diffusion of Cu atoms as a passivation layer. Similar observation has been reported for np-Au materials starting from Ag-rich alloys.<sup>60,61</sup> The spatial enrichment and distribution of less noble metal within np-materials might have a huge impact in heterogeneous and electrochemical catalysis to tune the electronic and geometric effects.

In alkaline media, the dealloying process is mainly restricted by the slow surface diffusion of Cu (hydr)oxide species,

forming when Cu atoms are in exposure to strongly alkaline solution. The surface diffusion coefficient of Cu (hydr)oxide species is suggested to be two to three magnitudes slower than metallic Cu.<sup>17,27,36,37</sup> It was also seen from the estimation of the surface diffusivity ( $D_s$ ) in HCl ( $1.4 \times 10^{-18} \text{ m}^2 \text{ s}^{-1}$ ) and NaOH ( $9.4 \times 10^{-21} \text{ m}^2 \text{ s}^{-1}$ ) at 25 °C in this work. This limits the coarsening process and leads to the formation of smaller ligaments compared to dealloying in acidic media. The slow Cu diffusion and evolution of small ligaments/pores restrict the dealloying front propagation in the thick ribbons. Therefore, the np structure only forms on the surface and the properties to the original master alloy retain in the bulk. On the other hand, during dealloying in strong alkaline media, low-coordinated Cu atoms dissolve in minor concentration and enrich near the alloy surface. We believe that over dealloying time the concentration of soluble Cu species gradually increases until a critical concentration has been achieved. Above this threshold (supersaturation), Cu species commence to re-deposit and grow as Cu(I)oxide crystals at the alloy surface. We suggest that the critical point of the supersaturation is different inside the pores rather than outside of the pores (bulk electrolyte). Therefore, we observed a sudden change in the morphological structure of np-Cu in NaOH due to the formation and growth of Cu(I)oxide seed crystals inside the pores.<sup>17</sup> Both the formation of octahedral  $\text{Cu}_2\text{O}$  crystals and the slow Cu surface diffusion hinder electrolyte penetration and thus the dealloying of the bulk ribbons.

We can sum up that dealloying conditions such as electrolyte and dealloying temperature strongly control the structure and the residual Zn content within the np-Cu ribbons.

#### 5. CONCLUSIONS

In this work, we studied the formation of np-Cu by chemical dealloying of  $Zn_{80}Cu_{20}$  alloy ribbons in two different electrolytes and pH values. The master alloy was prepared by melt spinning and the obtained alloy ribbons consist of a Zn-enriched surface layer (of  $\sim 14 \text{ nm}$ ), followed by a homogenous sub-surface and bulk composition. The chemical dealloying of the ribbons in 0.1 M HCl and 1.3 M NaOH leads to formation of an extended ligament-pore network with different structural and chemical properties. In particular, the dealloying process in HCl facilitates the Zn dissolution, resulting in a change of the crystal structure from hexagonal  $\text{Cu}_{20}\text{Zn}_{80}$  to cubic  $\text{Cu}_{38}\text{Zn}_{62}$  and finally to cubic Cu. Residuals of Zn of 1–2 at. % are enough to preserve the homogeneous ligament structure even after very long dealloying times (13 days). Very interestingly, the distribution of Zn within the single ligaments is inhomogeneous by the formation of local Zn-rich regions near the surface. The appearance of these Zn-rich regions might be very likely related to the passivation behavior of Cu surface atoms and might be relics of the master alloy.

In acidic environments, the ligament size and Zn content are strongly correlated to each other, as the ligament size grows and simultaneously the residual Zn content decreases over the dealloying time. On the other hand, ligaments formed in alkaline media are smaller and the ligament size is independent from the residual Zn content. Despite the relatively thick melt-spun ribbons ( $35 \pm 3 \mu\text{m}$ ), kinetics of a bicontinuous ligament-pore structure are controlled by the interfacial process instead of the diffusion of corrosive electrolyte solution in and out of the porous layers, referred to as long-range mass

transport. Surface diffusivities of Cu at 25 °C were determined to be  $1.4 \times 10^{-18}$  and  $9.4 \times 10^{-21}$  m<sup>2</sup> s<sup>-1</sup> in 0.1 M HCl and 1.3 M NaOH, respectively. Therefore, the high Cu surface diffusion rate in the presence of chloride ions enables an enhanced dealloying front propagation into the ribbons, and also coarsening of the ligaments to form larger ligament. On the contrary, the slow surface diffusion rate of Cu (hydr)oxide in 1.3 M NaOH solution strongly limits the dealloying process and forms smaller ligaments.

The effect of different dealloying conditions was also investigated. Agitation and de-aeration of the acidic electrolyte has no significant influence on the structure of np-Cu. On the other hand, dealloying temperature strongly influences the surface diffusivity of Cu, leading to a strong relationship between dealloying temperature and the np-Cu structure.

This study describes the formation of np-Cu materials with tunable ligament size and residual Zn content starting from alloy ribbons, which allows for tuning the structural and chemical properties of a np-Cu material for a wide range of possible applications in electrochemical synthesis, sensors and catalysis.

## ■ ASSOCIATED CONTENT

### SI Supporting Information

The Supporting Information is available free of charge at <https://pubs.acs.org/doi/10.1021/acs.jpcc.1c08258>.

Additional experimental parameters and spectra of XPS, some photographs of the Zn<sub>80</sub>Cu<sub>20</sub> ribbons, additional experimental results about the effect of agitation, de-aeration and dealloying temperature on the microstructure of np-Cu ribbons, ligament size distributions, *i*R-corrected polarization curves for HER on pure Cu, Zn and Zn<sub>80</sub>Cu<sub>20</sub> alloy ribbon, and comparison with the reported literature of np-Cu prepared by dealloying (PDF)

## ■ AUTHOR INFORMATION

### Corresponding Author

**Mehtap Oezaslan** – Institute of Chemistry, Carl von Ossietzky University of Oldenburg, 26129 Oldenburg, Germany; Technical Electrocatalysis Laboratory, Institute of Technical Chemistry, Technical University of Braunschweig, 38106 Braunschweig, Germany; [orcid.org/0000-0001-8545-7576](https://orcid.org/0000-0001-8545-7576); Email: [m.oezaslan@tu-braunschweig.de](mailto:m.oezaslan@tu-braunschweig.de)

### Authors

**Sawsan Ibrahim** – Institute of Chemistry, Carl von Ossietzky University of Oldenburg, 26129 Oldenburg, Germany; Technical Electrocatalysis Laboratory, Institute of Technical Chemistry, Technical University of Braunschweig, 38106 Braunschweig, Germany; [orcid.org/0000-0001-6721-8635](https://orcid.org/0000-0001-6721-8635)

**Alexandra Dworzak** – Institute of Chemistry, Carl von Ossietzky University of Oldenburg, 26129 Oldenburg, Germany; Technical Electrocatalysis Laboratory, Institute of Technical Chemistry, Technical University of Braunschweig, 38106 Braunschweig, Germany

**Daniel Crespo** – Departament de Física, Institut de Tècniques Energètiques and Barcelona Research Center in Multiscale Science and Engineering, Universitat Politècnica de Catalunya, 08019 Barcelona, Spain; [orcid.org/0000-0003-1743-2400](https://orcid.org/0000-0003-1743-2400)

**Frank Uwe Renner** – Institute for Materials Research (IMO), Hasselt University, 3500 Hasselt, Belgium; Division IMOMEC, IMEC VZW, 3590 Diepenbeek, Belgium;

[orcid.org/0000-0003-0425-393X](https://orcid.org/0000-0003-0425-393X)

**Carsten Dosche** – Institute of Chemistry, Carl von Ossietzky University of Oldenburg, 26129 Oldenburg, Germany;

[orcid.org/0000-0003-3837-5169](https://orcid.org/0000-0003-3837-5169)

Complete contact information is available at: <https://pubs.acs.org/doi/10.1021/acs.jpcc.1c08258>

## Notes

The authors declare no competing financial interest.

## ■ ACKNOWLEDGMENTS

Financial support from the Deutsche Forschungsgesellschaft (DFG, GRK 2226), DFG research unit (FOR2213 under contract number OE610/1-1, [www.nagocat.de](http://www.nagocat.de)), and Bundesministerium für Bildung und Forschung (BMBF, FKZ 03SF0539) are gratefully acknowledged. Furthermore, we thank the DFG for funding the JEOL JEM2100F TEM (INST 184/106-1 FUGG), ESCALAB 250 Xi XPS spectrometer (INST 184/144-1 FUGG) and Empyrean  $\theta$ - $\theta$  diffractometer Panalytical (INST 184/154-1 FUGG). The authors also acknowledge the Electron and Light Microscopy Service Unit, Carl von Ossietzky University of Oldenburg, Germany. D.C. acknowledges the funding from MICINN (grant FIS2017-82625-P) and Generalitat de Catalunya (grant 2017SGR0042).

## ■ REFERENCES

- (1) McCue, I.; Benn, E.; Gaskey, B.; Erlebacher, J. Dealloying and Dealloyed Materials. *Annu. Rev. Mater. Res.* **2016**, *46*, 263–286.
- (2) Juarez, T.; Biener, J.; Weissmüller, J.; Hodge, A. M. Nanoporous metals with structural hierarchy: A review. *Adv. Eng. Mater.* **2017**, *19*, 1700389.
- (3) Wittstock, A.; Biener, J.; Bäumer, M. Surface Chemistry and Catalysis. In *Nanoporous Gold: From an Ancient Technology to a High-Tech Material*; RSC Nanoscience & Nanotechnology; Royal Society of Chemistry, 2012; Vol. 22, pp 167–198.
- (4) Wang, L.-C.; Stowers, K. J.; Zugic, B.; Personick, M. L.; Biener, M. M.; Biener, J.; Friend, C. M.; Madix, R. J. Exploiting basic principles to control the selectivity of the vapor phase catalytic oxidative cross-coupling of primary alcohols over nanoporous gold catalysts. *J. Catal.* **2015**, *329*, 78–86.
- (5) Qiu, H.-J.; Ito, Y.; Chen, M. W. Hierarchical nanoporous nickel alloy as three-dimensional electrodes for high-efficiency energy storage. *Scr. Mater.* **2014**, *89*, 69–72.
- (6) Lang, X. Y.; Yuan, H. T.; Iwasa, Y.; Chen, M. W. Three-dimensional nanoporous gold for electrochemical supercapacitors. *Scr. Mater.* **2011**, *64*, 923–926.
- (7) Diao, F.; Xiao, X.; Luo, B.; Sun, H.; Ding, F.; Ci, L.; Si, P. Two-step fabrication of nanoporous copper films with tunable morphology for SERS application. *Appl. Surf. Sci.* **2018**, *427*, 1271–1279.
- (8) Cialone, M.; Celegato, F.; Scaglione, F.; Barrera, G.; Raj, D.; Coisson, M.; Tiberto, P.; Rizzi, P. Nanoporous FePd alloy as multifunctional ferromagnetic SERS-active substrate. *Appl. Surf. Sci.* **2021**, *543*, 148759.
- (9) Chen, L. Y.; Lang, X. Y.; Fujita, T.; Chen, M. W. Nanoporous gold for enzyme-free electrochemical glucose sensors. *Scr. Mater.* **2011**, *65*, 17–20.
- (10) Rebbecchi, T. A.; Chen, Y. Template-based fabrication of nanoporous metals. *J. Mater. Res.* **2018**, *33*, 2–15.
- (11) Song, T.; Yan, M.; Qian, M. The enabling role of dealloying in the creation of specific hierarchical porous metal structures—A review. *Corros. Sci.* **2018**, *134*, 78–98.

- (12) Erlebacher, J.; Aziz, M. J.; Karma, A.; Dimitrov, N.; Sieradzki, K. Evolution of nanoporosity in dealloying. *Nature* **2001**, *410*, 450–453.
- (13) Weissmüller, J.; Newman, R. C.; Jin, H.-J.; Hodge, A. M.; Kysar, J. W. Nanoporous Metals by Alloy Corrosion: Formation and Mechanical Properties. *MRS Bull.* **2009**, *34*, 577–586.
- (14) Pickering, H. W.; Wagner, C. Electrolytic dissolution of binary alloys containing a noble metal. *J. Electrochem. Soc.* **1967**, *114*, 698.
- (15) Zhang, Z.; Wang, Y.; Qi, Z.; Zhang, W.; Qin, J.; Frenzel, J. Generalized Fabrication of Nanoporous Metals (Au, Pd, Pt, Ag, and Cu) through Chemical Dealloying. *J. Phys. Chem. C* **2009**, *113*, 12629–12636.
- (16) Egle, T.; Barroo, C.; Janvelyan, N.; Baumgaertel, A. C.; Akey, A. J.; Biener, M. M.; Friend, C. M.; Bell, D. C.; Biener, J. Multiscale Morphology of Nanoporous Copper Made from Intermetallic Phases. *ACS Appl. Mater. Interfaces* **2017**, *9*, 25615–25622.
- (17) Hecker, B.; Dosche, C.; Oezaslan, M. Ligament evolution in nanoporous Cu films prepared by dealloying. *J. Phys. Chem. C* **2018**, *122*, 26378–26384.
- (18) Zhang, L.; Chen, L.; Liu, H.; Hou, Y.; Hirata, A.; Fujita, T.; Chen, M. Effect of Residual Silver on Surface-Enhanced Raman Scattering of Dealloyed Nanoporous Gold. *J. Phys. Chem. C* **2011**, *115*, 19583–19587.
- (19) Kim, S. H. Nanoporous gold: Preparation and applications to catalysis and sensors. *Curr. Appl. Phys.* **2018**, *18*, 810–818.
- (20) Badwe, N.; Chen, X.; Sieradzki, K. Mechanical properties of nanoporous gold in tension. *Acta Mater.* **2017**, *129*, 251–258.
- (21) Xiao, X.; Si, P.; Magner, E. An overview of dealloyed nanoporous gold in bioelectrochemistry. *Bioelectrochemistry* **2016**, *109*, 117–126.
- (22) Xie, Y.; Dimitrov, N. Ultralow Pt loading nanoporous Au-Cu-Pt thin film as highly active and durable catalyst for formic acid oxidation. *Appl. Catal., B* **2020**, *263*, 118366.
- (23) Hwang, C. K.; Kim, J. M.; Hwang, S.; Kim, J. H.; Sung, C. H.; Moon, B. M.; Chae, K. H.; Singh, J. P.; Kim, S. H.; Jang, S. S.; Lee, S. W.; Ham, H. C.; Han, S.; Kim, J. Y. Porous Strained Pt Nanostructured Thin-Film Electrocatalysts via Dealloying for PEM Fuel Cells. *Adv. Mater. Interfaces* **2020**, *7*, 1901326.
- (24) Zhu, D.; Xia, C.; Yang, Z.; Wang, X.; Yang, T.; Liang, C.; Yin, F.; Li, Q. Fabrication of non-enzyme glucose sensor via dealloying amorphous Zr-Cu alloy and anodic oxidation. *Mater. Lett.* **2019**, *245*, 49–52.
- (25) Liu, W.; Chen, L.; Yan, J.; Li, N.; Shi, S.; Zhang, S. Nanoporous copper from dual-phase alloy families and its technology application in lithium ion batteries. *Corros. Rev.* **2015**, *33*, 203–231.
- (26) Heßelmann, C.; Wolf, T.; Galgon, F.; Körner, C.; Albert, J.; Wasserscheid, P. Additively manufactured RANEY-type copper catalyst for methanol synthesis. *Catal. Sci. Technol.* **2020**, *10*, 164–168.
- (27) Li, M.; Zhou, Y.; Geng, H. Fabrication of nanoporous copper ribbons by dealloying of Al-Cu alloys. *J. Porous Mater.* **2012**, *19*, 791–796.
- (28) Dan, Z.; Qin, F.; Sugawara, Y.; Muto, I.; Hara, N. Fabrication of nanoporous copper by dealloying amorphous binary Ti-Cu alloys in hydrofluoric acid solutions. *Intermetallics* **2012**, *29*, 14–20.
- (29) Li, A.; Geng, H.; Zhou, Y.; Ding, L. Fabrication of nanoporous copper ribbons by dealloying of Mn<sub>70</sub>Cu<sub>30</sub> alloy and fractal characterization of their porosity. *Rev. Adv. Mater. Sci.* **2013**, *33*, 56–60.
- (30) Liu, W.; Zhang, S.; Li, N.; An, S.; Zheng, J. Formation of monolithic nanoporous copper with ultrahigh specific surface area through chemical dealloying of Mg-Cu alloy. *Int. J. Electrochem. Sci.* **2012**, *7*, 9707–9716.
- (31) Jia, F.; Yu, C.; Deng, K.; Zhang, L. Nanoporous Metal (Cu, Ag, Au) Films with High Surface Area: General Fabrication and Preliminary Electrochemical Performance. *J. Phys. Chem. C* **2007**, *111*, 8424–8431.
- (32) Vivegnis, S.; Delhalle, J.; Mekhalif, Z.; Renner, F. U. Copper-zinc alloy electrodeposition mediated by triethanolamine as a complexing additive and chemical dealloying. *Electrochim. Acta* **2019**, *319*, 400–409.
- (33) Hayes, J. R.; Hodge, A. M.; Biener, J.; Hamza, A. V.; Sieradzki, K. Monolithic nanoporous copper by dealloying Mn-Cu. *J. Mater. Res.* **2006**, *21*, 2611–2616.
- (34) Qi, Z.; Zhao, C.; Wang, X.; Lin, J.; Shao, W.; Zhang, Z.; Bian, X. Formation and Characterization of Monolithic Nanoporous Copper by Chemical Dealloying of Al-Cu Alloys. *J. Phys. Chem. C* **2009**, *113*, 6694–6698.
- (35) Scaglione, F.; Rizzi, P.; Battezzati, L. De-alloying kinetics of an Au-based amorphous alloys. *J. Alloys Compd.* **2012**, *536*, S60–S64.
- (36) Liu, W. B.; Zhang, S. C.; Li, N.; Zheng, J. W.; Xing, Y. L. Facile One-Pot Synthesis of Nanoporous Copper Ribbons with Bimodal Pore Size Distributions by Chemical Dealloying. *J. Electrochem. Soc.* **2011**, *158*, D611.
- (37) Liu, W.; Chen, L.; Yan, J.; Li, N.; Shi, S.; Zhang, S. Dealloying solution dependence of fabrication, microstructure and porosity of hierarchical structured nanoporous copper ribbons. *Corros. Sci.* **2015**, *94*, 114–121.
- (38) Darque-Ceretti, E.; Delamare, F.; Blaise, G. Ion induced surface compositional changes of  $\alpha$  brass; a comparative study by AES and sputtered thermal ion mass spectrometry. Application to quantitative AES. *Surf. Interface Anal.* **1985**, *7*, 141–149.
- (39) Van Ooij, W. J. Surface composition, oxidation and sulfidation of cold-worked brass and brass-coated steel wire as studied by x-ray photoelectron spectroscopy I. Surface composition of commercial cold-worked brass. *Surf. Technol.* **1977**, *6*, 1–18.
- (40) Haynes, W. M. *CRC Handbook of Chemistry and Physics*; CRC Press, 2014.
- (41) Gražulis, S.; Chateigner, D.; Downs, R. T.; Yokochi, A.; Quirós, M.; Lutterotti, L.; Manakova, E.; Butkus, J.; Moeck, P.; Le Bail, A. Crystallography Open Database—an open-access collection of crystal structures. *J. Appl. Crystallogr.* **2009**, *42*, 726–729.
- (42) Zuo, J.; Erbe, A. Optical and electronic properties of native zinc oxide films on polycrystalline Zn. *Phys. Chem. Chem. Phys.* **2010**, *12*, 11467–11476.
- (43) Liu, Y.; Liu, Y.; Yang, Z.; Wang, J. Fenton degradation of 4-chlorophenol using H<sub>2</sub>O<sub>2</sub> in situ generated by Zn-CNTs/O<sub>2</sub> system. *RSC Adv.* **2017**, *7*, 49985–49994.
- (44) Lu, Z.; Li, C.; Han, J.; Zhang, F.; Liu, P.; Wang, H.; Wang, Z.; Cheng, C.; Chen, L.; Hirata, A. Three-dimensional bicontinuous nanoporous materials by vapor phase dealloying. *Nat. Commun.* **2018**, *9*, 276.
- (45) Kong, Q.; Lian, L.; Liu, Y.; Zhang, J. Hierarchical porous copper materials: fabrication and characterisation. *Micro Nano Lett.* **2013**, *8*, 432–435.
- (46) Lian, L.; Yao, Y.; Liu, Y.; Fang, X. A segmental dealloying for fabricating the gradient nanoporous metal materials. *J. Porous Mater.* **2017**, *24*, 211–215.
- (47) Morrish, R.; Dorame, K.; Muscat, A. J. Formation of nanoporous Au by dealloying AuCu thin films in HNO<sub>3</sub>. *Scr. Mater.* **2011**, *64*, 856–859.
- (48) Chung, Y.-C.; Kim, C. K.; Wuensch, B. J. Calculation of the contribution to grain boundary diffusion in ionic systems that arises from enhanced defect concentrations adjacent to the boundary. *J. Appl. Phys.* **2000**, *87*, 2747–2752.
- (49) Liu, W.; Zhang, S.; Li, N.; Zheng, J.; An, S.; Xing, Y. Monolithic nanoporous copper ribbons from Mg-Cu alloys with copper contents below 33 at.-%: fabrication, structure evolution and coarsening behavior along the thickness direction. *Int. J. Electrochem. Sci.* **2011**, *6*, 5445–5461.
- (50) Erlebacher, J. An Atomistic Description of Dealloying. *J. Electrochem. Soc.* **2004**, *151*, C614.
- (51) Wang, N.; Pan, Y.; Wu, S.; Zhang, E.; Dai, W. Fabrication of nanoporous copper with tunable ligaments and promising sonocatalytic performance by dealloying Cu-Y metallic glasses. *RSC Adv.* **2017**, *7*, 43255–43265.
- (52) Dan, Z.; Qin, F.; Sugawara, Y.; Muto, I.; Hara, N. Dependency of the formation of Au-stabilized nanoporous copper on the

dealloying temperature. *Microporous Mesoporous Mater.* **2014**, *186*, 181–186.

(53) Qian, L. H.; Chen, M. W. Ultrafine nanoporous gold by low-temperature dealloying and kinetics of nanopore formation. *Appl. Phys. Lett.* **2007**, *91*, 083105.

(54) Dan, Z.; Qin, F.; Muto, I.; Hara, N.; Chang, H. Elaboration of Nanoporous Copper via Chemical Composition Design of Amorphous Precursor Alloys. In *New Uses of Micro and Nanomaterials*; Books on Demand, 2018; p 39.

(55) Aburada, T.; Fitz-Gerald, J. M.; Scully, J. R. Synthesis of nanoporous copper by dealloying of Al-Cu-Mg amorphous alloys in acidic solution: The effect of nickel. *Corros. Sci.* **2011**, *53*, 1627–1632.

(56) Wang, Y.; Wang, Y.; Zhang, C.; Kou, T.; Zhang, Z. Tuning the ligament/channel size of nanoporous copper by temperature control. *CrystEngComm* **2012**, *14*, 8352–8356.

(57) Lee, Y.-Z.; Zeng, W.-Y.; Cheng, I.-C. Synthesis and characterization of nanoporous copper thin films by magnetron sputtering and subsequent dealloying. *Thin Solid Films* **2020**, *699*, 137913.

(58) Zhang, X.-m.; Li, Y.-x.; Zhang, H.-w.; Liu, Y. Evolution of porous structure with dealloying corrosion on Gasar Cu–Mn alloy. *Trans. Nonferrous Met. Soc. China* **2015**, *25*, 1200–1205.

(59) Erlebacher, J. An atomistic description of dealloying: porosity evolution, the critical potential, and rate-limiting behavior. *J. Electrochem. Soc.* **2004**, *151*, C614.

(60) Krekeler, T.; Straßer, A. V.; Graf, M.; Wang, K.; Hartig, C.; Ritter, M.; Weissmüller, J. Silver-rich clusters in nanoporous gold. *Mater. Res. Lett.* **2017**, *5*, 314–321.

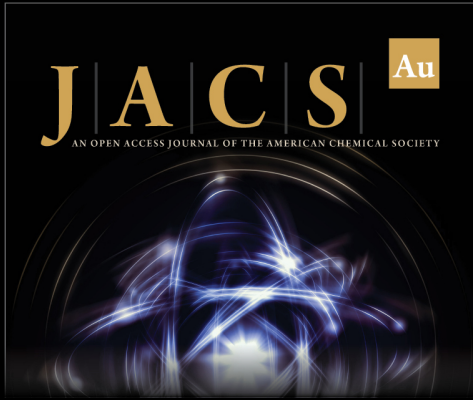
(61) Mahr, C.; Kundu, P.; Lackmann, A.; Zanaga, D.; Thiel, K.; Schowalter, M.; Schwan, M.; Bals, S.; Wittstock, A.; Rosenauer, A. Quantitative determination of residual silver distribution in nanoporous gold and its influence on structure and catalytic performance. *J. Catal.* **2017**, *352*, 52–58.

(62) Chen-Wiegart, Y.-c. K.; Wang, S.; Lee, W.-K.; McNulty, I.; Voorhees, P. W.; Dunand, D. C. In situ imaging of dealloying during nanoporous gold formation by transmission X-ray microscopy. *Acta Mater.* **2013**, *61*, 1118–1125.

(63) Chen-Wiegart, Y.-c. K.; Wang, S.; McNulty, I.; Dunand, D. C. Effect of Ag–Au composition and acid concentration on dealloying front velocity and cracking during nanoporous gold formation. *Acta Mater.* **2013**, *61*, 5561–5570.


(64) Policastro, S. A.; Carnahan, J. C.; Zangari, G.; Bart-Smith, H.; Seker, E.; Begley, M. R.; Reed, M. L.; Reynolds, P. F.; Kelly, R. G. Surface Diffusion and Dissolution Kinetics in the Electrolyte–Metal Interface. *J. Electrochem. Soc.* **2010**, *157*, C328.


(65) Wang, J.; Yang, S. Nanoporous copper fabricated by dealloying Mn–Cu precursors with minor nickel element addition and heat treatment coarsening. *Nano* **2018**, *13*, 1850058.



**JACS** Au  
AN OPEN ACCESS JOURNAL OF THE AMERICAN CHEMICAL SOCIETY

Editor-in-Chief  
**Prof. Christopher W. Jones**  
Georgia Institute of Technology, USA

**Open for Submissions** 

pubs.acs.org/jacsau  ACS Publications  
Most Trusted. Most Cited. Most Read.